Springer

KSME

Journal of Mechanical Science and Technology 24 (9) (2010) 1781~1791
www.springerlink.com/content/1738-494x
DOI 10.1007/s12206-010-0610-2

Performance characterization of a small-capacity thermoacoustic cooler for air-conditioning applications †

Insu Paek[1,*], Luc Mongeau[2] and James E. Braun[3]

[1]*Department of Mechanical and Mechatronics Engineering, Kangwon National University, Chuncheon, Gangwondo, 200-701, Korea*
[2]*Department of Mechanical Engineering, McGill University, Montreal, QC H3A 2K6, Canada*
[3]*School of Mechanical Engineering, Purdue University, West Lafayette, IN 47907, USA*

(Manuscript Received December 28, 2009; Revised June 1, 2010; Accepted June 1, 2010)

Abstract

The performance of a working prototype, operated with and without water flow through the heat exchangers, was measured and found to be in reasonably close agreement to predictions from a simulation code, DELTAE, based on linear thermoacoustic theory. Further analysis and DELTAE simulations showed that the coefficient of performance may be significantly reduced when the stack temperature profile becomes non-linear, i.e. when the system is operated for a temperature span smaller than the optimal value for a given stack length. Guidelines to avoid this condition are provided.

Keywords: Thermoacoustic cooling; Performance; Stack; Temperature; Simulation

1. Introduction

Standing wave thermoacoustic cooling is achieved through the utilization of the energy in acoustic standing waves [1]. Periodic compression and expansion of gas, combined with heat transfer with solid, results in heat pumping from pressure node to pressure antinode.

Standing wave thermoacoustic coolers developed so far were designed to target relatively low cooling temperatures, mostly for refrigeration applications. This required a relatively long stack compared with the resonator length, and a limited cooling load. For this reason, some standing wave thermoacoustic coolers could reach temperatures well below the freezing temperature of water but with cooling capacities less than 10 W [2-5]. Heat exchangers with a secondary fluid flow loop have not been used in most previous studies, in part due to the low cooling capacity considered.

The cooling capacity of standing wave thermoacoustic coolers has increased over recent years, as design efforts are being made to improve system performance [6-8] and find the best possible application for these systems [9]. Relatively high cooling loads and efficient cooling requires fin and tube heat exchangers with secondary fluid flow [6-8]. The largest-capacity standing-wave thermoacoustic cooler to date achieved more than 2 kW of cooling power with a cold-side temperature of 10.4 °C [8].

The relatively sparse use of thermoacoustic coolers with secondary loop heat exchangers designed for low temperature lifts has resulted in a scarcity of investigations of the temperature profile along the stack and its effects on system performance. Wheatley at al. experimentally investigated the temperature profile along a thermoacoustic couple using a U-shape standing wave thermoacoustic cooler [10]. They showed that the temperature profile obeys an exponential decay curve when the temperature gradient across the thermoacoustic couple is close to a critical temperature gradient where the cooling capacity goes to zero. No detailed investigations have been reported for other conditions of interest for low temperature lift, moderate capacity applications.

The purpose of this study was to characterize the performance of a standing-wave thermoacoustic cooler, in particular focusing on the role of the temperature profile along the stack. A standing-wave thermoacoustic cooler designed for a small-capacity air-conditioning application with a relatively short stack was used. Performance measurements with and without water flow through the cold-side heat exchanger were made. The relation between system performance and stack temperature profile was established for various operating conditions, both for experimental data and numerical simulations. A reversal of the temperature gradient within the stack was observed over the hot end of the stack in some conditions. Theoretical models are presented to explain the results, and establish limits over which this regime may be encountered.

† This paper was recommended for publication in revised form by Associate Editor Yeon June Kang

* Corresponding author. Tel.: +82 33 250 6379, Fax: +82 33 257 4190
E-mail address: paek@kangwon.ac.kr

Table 1. Key dimensions of the vessel, in millimeters.

Section	Upstream Diameter	Downstream Diameter	Length
Back Cavity	168	163	203
Driver Housing	89	114	184
Conical Enlargement	93	152	85
Hot Heat Exchanger	152	161	25
Stack	161	161	25
Cold Heat Exchanger	161	152	25
Conical Reduction	152	67	136
Resonator Tube	67	67	743

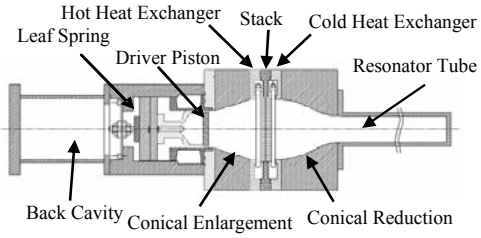

Fig. 1. Schematic of the standing wave thermoacoustic cooler. Dimensions of the parts are listed in Table 1.

2. Experimental apparatus

2.1 Description of the thermoacoustic cooling system

A schematic of the prototype used in this study is shown in Fig.1. The device, which is approximately one half-wavelength long, was designed for operation in a nominally 55% helium-45% argon mixture, and the operating frequency was near 170 Hz [11]. The system is comprised of an electrodynamic linear actuator (or driver), two heat exchangers, the heat pumping element (stack), and the resonator system within an enclosed, sealed vessel. Key dimensions of the inside cross-section of the vessel are listed in Table 1.

2.2 The vessel

The system is made of aluminum modular sections, connected using high-strength bolts. The main sections include, from left to right in Fig. 1, the back cavity, the driver, the area expansion, the hot heat exchanger, the stack, the cold heat exchanger, the area contraction, and finally the resonator. O-ring seals prevent leakage between each section. All sections with the exception of the driver/back cavity and the resonator are assembled in a sandwich construction, and maintained using the aforementioned bolts.

2.3 The driver and power source

The system is driven by a moving-magnet electromechanical transducer (CFIC Model B-300). The driver can provide up to about 210 W of acoustic power at 33 Hz, with an electro-acoustic transduction efficiency of 70 % and a maximum displacement of 6 mm. More information on the driver

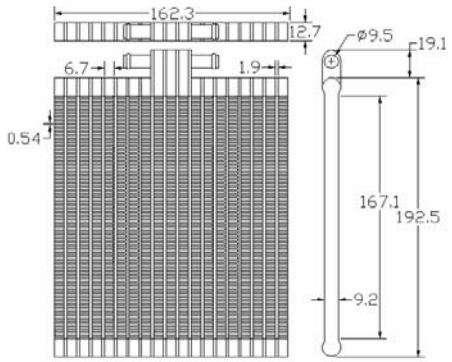

Fig. 2. Schematic of the heat exchanger (dimensions in millimeters).

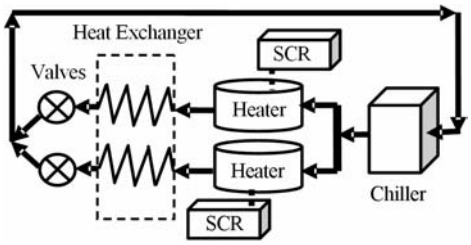

Fig. 3. Schematic of the temperature controlled closed water loop. The flow direction is described by the arrows.

characteristics is available in Yarr and Corey [12]. Leaf springs were added in this study to increase the mechanical resonance frequency of the driver in-vacuo to 163 Hz. The operating frequency used ranged between 157.4 Hz and 172 Hz depending on the gas mixture and the mean pressure. The increase in operating frequency increased the electrical resistance of the coil in the driver and reduced the maximum electroacoustic efficiency to 61 % [13]. A single-frequency sinusoidal signal was fed to a power amplifier (Techron Model 5330) using a signal generator (Agilent E-1432A). Detailed information of the characteristics of the driver is available [13].

2.4 The stack

The stack is made of a 76 μm thick polyester film, and 254 μm thick nylon wire constructed by using the wire as a spacer and rolling the film into a cylinder. The wire adheres to the film crosswise and the 2.54 cm wide film is then rolled up, resulting in thousands of small parallel channels in which the gas oscillates. The spacing between the nylon wire varied between a few millimeters and a few centimeters. The diameter of the stack section was about 161 cm.

2.5 The heat exchanger and secondary water loop

Two identical custom-made fin-tube heat exchangers were used as the hot and cold heat exchangers. They were made of aluminum and had tubes 1.9 mm wide and 7.9 mm deep. The fin spacing of the heat exchanger was 0.54 mm. The schematic of the heat exchanger is shown in Fig. 2.

A temperature controlled water loop as shown in Fig. 3 was

used to control boundary conditions for the heat exchangers. The water temperatures were controlled by a chiller (Tek-Temp Instrument, TKD-100) and two water heaters (Vanguard, 81VP15S) using silicon controlled rectifier power controllers (Cristal Controls, CCPA-30-1-A-S3). Detailed information about the heat exchangers and the water loop is available in Ref. 11.

3. Measurement procedures and experimental verifications

The frequency of the input signal was varied in order to find the resonance frequency of the system. For all the measurements, the driver was operated at frequencies near the acoustic resonance of the system for consistency. The electroacoustic efficiencies for most cases were higher at frequencies off the resonance because the mechanical resonance frequency of the driver did not match the acoustic resonance frequency [13, 14].

3.1 Instrumentation

Temperature, differential temperature, water flow rate, acoustic pressure, and acceleration signals were measured to evaluate the acoustic power and heat exchange rates. Arrays of four Type T thermocouples (Omega, fine wire type) having uncertainties of 0.5 C were positioned to capture the average gas temperatures near the ends of the stack and the exchangers. Within the secondary water loop, type T thermocouple probes (Omega) and differential thermopiles (Delta-T Company 75X) were installed to measure the temperature change of the water between inlet and outlet of each exchanger. The sensor uncertainties were 0.5 C and 0.08 C, respectively. The volume flow rate of water through each heat exchanger was measured with precision axial paddle wheel turbine type flow meters (JLC International IR-Opflow). The uncertainty of the flow meter was 0.01 % of the measured value. The differential temperature of water across the heat exchangers was used to evaluate the heat delivery to the gas in the cold exchanger and the heat rejection from the gas in the hot exchanger. A piezoelectric dynamic pressure sensor (PCB, 102A03) in a port near the piston was used to measure driver acoustic pressure. An accelerometer (PCB, 353B13) mounted on the carriage of the linear motor was used to measure piston acceleration. The input acoustic power was calculated based on accelerometer and driver pressure signals. The electrical power input to the driver was estimated by using the voltage of the driver coil measured with a voltage divider, and the coil current measured using a current probe. All the measured data were recorded. More detailed information about the instrumentation is available in Ref. 11.

3.2 Experimental accuracy

To check the accuracy of the experimental data, the relative uncertainty in the estimated heat transfer rates, and the thermodynamic first law imbalances of the heat transfer rates and the acoustic power were calculated. The heat transfer rate on either the hot or the cold side was estimated using [15]

$$\dot{Q} = \rho_w \dot{V}_w C_w \Delta T_w , \tag{1}$$

where, $\dot{Q}$ is the heat transfer rate, ρ_w is the density of water, $\dot{V}_w$ is the volume flow rate of water, C_w is the specific heat of water, and ΔT_w is the differential water temperature across the heat exchanger. Using the known uncertainties of the sensors for temperature, differential temperature, and volume flow rate, the relative uncertainty (or fractional uncertainty) of the heat transfer rate estimate was calculated from [16]:

$$\delta_R \dot{Q} = \frac{\delta \dot{Q}}{\dot{Q}} = \sqrt{\left(\frac{\delta \dot{V}_w}{\dot{V}_w}\right)^2 + \left(\frac{\delta \rho_w}{\rho_w}\right)^2 + \left(\frac{\delta \Delta T_w}{\Delta T_w}\right)^2} . \tag{2}$$

In Eq. (2), δ and δ_R denote absolute and relative uncertainties, respectively. The contribution from the density is small compared to other terms; therefore it was neglected.

As another verification of the measured data, especially for the measurement with water flow through the cold-side heat exchanger, the thermodynamic first law imbalance ratio was also calculated. The metric for the overall data accuracy, is defined as

$$Imb(\%) = \frac{\left|\dot{W}_{ac} + |\dot{Q}_c| - |\dot{Q}_h|\right|}{\dot{W}_{ac} + |\dot{Q}_c|} , \tag{3}$$

where Imb is the imbalance ratio, $\dot{W}_{ac}$ is the measured acoustic power near piston, $\dot{Q}_c$ is the heat-transfer rate at the cold side heat exchanger, and $\dot{Q}_h$ is the heat-transfer rate at the hot side heat exchanger.

4. Overall system performance

4.1 Measurements without water flow through the cold-side heat exchanger

The overall performance of the thermoacoustic cooler was measured without water flow through the cold-side heat exchanger. The cold-side heat exchanger was placed next to the stack, disconnected from the water loop. The water inside the cold-side heat exchanger was evacuated. Two different helium and argon mixtures (55 % helium and 44 % helium) were used at a gauge mean pressure of 0.690 MPa.

The room temperature was initially measured. The hot-side water temperature was then set to the measured room temperature, through the use of an SCR power controller. Relatively high water flow rates ranging between 29 ml/s and 42 ml/s were chosen for the hot-side heat exchanger to ensure effective heat transfer between the hot-side stack end and the heat exchanger and to minimize any heat flow from the hot-side stack end to the cold side.

Acoustic power from the driver and the heat transfer rate through the hot-side heat exchanger were determined by using the measured water flow rate, the differential water tem-

Table 2. Measured data without water flow through cold heat exchanger. All the data were obtained at a mean pressure of 0.69 MPa.

No	He %	$\dot{W}_{ac}$ (W)	η_{DR} (%)	$\dot{Q}_h$ (W)	$\dot{Q}_h - \dot{W}_{ac}$ (W)	COP	Tgh (K)	Tgc (K)	DR (%)	$\delta_R \dot{Q}_h$ (%)
1	55	15.00	52.4	43.3	28.3	1.89	295.9	288.4	4.6	15.4
2	55	24.71	52.5	63.5	38.8	1.57	296.1	287.1	5.8	10.3
3	55	31.81	52.6	73.6	41.8	1.31	296.4	286.5	6.5	8.9
4	44	10.10	50.2	30.7	20.6	2.04	295.2	288.9	4.0	22.3
5	44	15.30	50.4	41.8	26.5	1.73	295.3	287.8	4.9	16.7
6	44	24.58	50.2	59.4	34.8	1.42	295.4	286.4	6.0	11.8
7	44	32.03	49.7	69.6	37.6	1.17	295.8	285.8	6.8	10.1
8	44	42.32	48.6	84.4	42.1	0.99	295.9	284.9	7.6	8.2
9	55	15.12	46.8	38.6	23.5	1.56	295.2	287.5	4.6	13.0
10	55	25.08	46.7	56.4	31.4	1.25	295.5	286.1	5.7	8.7
11	55	33.46	46.3	70.0	36.5	1.09	295.6	285.4	6.5	7.1
12	55	44.23	45.3	81.5	37.3	0.84	296.1	284.8	7.4	6.1
13	55	10.21	47.2	33.3	23.1	2.26	294.9	288.6	3.8	20.0
14	55	15.98	47.5	42.2	26.2	1.64	295.3	287.5	4.7	16.0
15	55	25.17	47.6	58.7	33.5	1.33	295.5	286.3	5.8	11.5
16	55	33.67	47.2	72.2	38.5	1.14	295.6	285.4	6.5	9.4
17	55	44.57	45.5	87.4	42.8	0.96	295.8	284.6	7.4	7.8

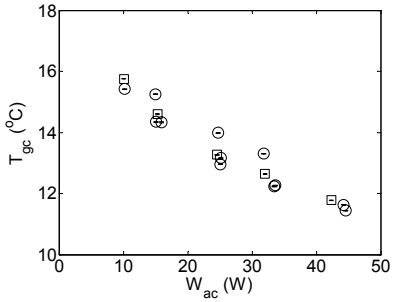

Fig. 4. Measured cold-side stack-end gas temperature vs. acoustic power input. No water flow through cold heat exchanger. O: 55 % helium and 45 % argon mixture, : 44 % helium and 56 % argon mixture. Data are plotted with error bars.

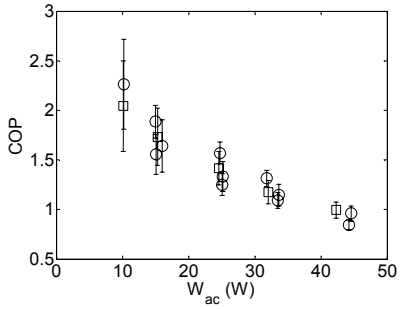

Fig. 5. COP vs. acoustic power input. No water flow through cold heat exchanger. O: 55 % helium and 45 % argon mixture, : 44 % helium and 56 % argon mixture. Data are plotted with error bars.

perature, the acoustic pressure at the driver, and the acceleration of the piston. The coefficient of performance (COP) of the thermoacoustic cooler was estimated from the acoustic power input and the measured hot-side heat transfer rate [15] by using

$$COP = \frac{\dot{Q}_h - \dot{W}_{ac}}{\dot{W}_{ac}} . \quad (4)$$

4.1.1 Experimental results

Table 2 shows the measured properties and calculated quantities. For all cases, the relative uncertainties in hot-side heat transfer rates, $\delta_R \dot{Q}_h$, estimated using (2) were less than 23 %. Most of the uncertainties resulted from small differential water temperatures. The cold-side stack-end gas temperature is plotted with respect to the acoustic power input in Fig. 4. As the acoustic power increased, the gas temperature decreased. When the acoustic power was about 42 W, the gas temperature reached 11.8 °C. For the data sets in Fig. 4, the electroacoustic efficiency varied between 45.3 % and 52.6 %. The room temperature for all the data points measured on four different days varied between 21.9 °C and 23.4 °C. The imbalance heat, defined as the difference between the measured hot-side heat transfer rate and the acoustic power input, is then indicative of the total heat transferred from the cold side along the stack. This quantity can be considered the cooling load to the system. The COP was calculated based on the imbalance heat and plotted with respect to the acoustic power input in Fig. 5. As expected, the COP decreased as the acoustic power increased.

4.1.2 Comparisons with linear acoustic model predictions

Efforts were made to compare the experimental results with

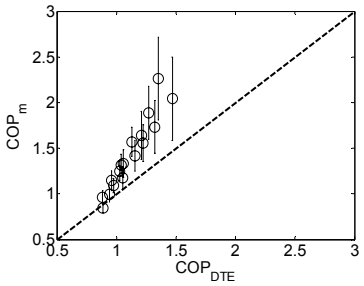

Fig. 6. Measured COP vs. COP obtained from DELTAE. Dashed line denotes the perfect agreement line. Data are plotted with error bars.

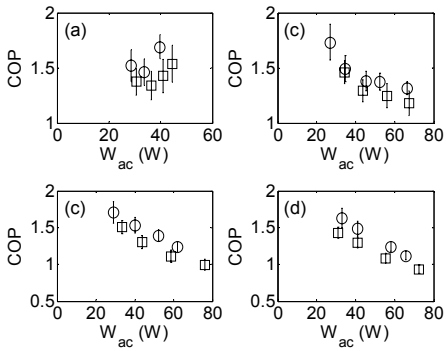

Fig. 7. COP vs. acoustic power input for various mean pressures. (a): 0.345 MPa, (b): 0.67 MPa, (c): 1.005 MPa and (d): 1.34 MPa. O: 55 % helium and 45 % argon mixture, : 44 % helium and 56 % argon mixture. All pressures are in gauge pressure. Data are plotted with error bars.

predictions from a computer model, DELTAE, based on linear acoustic theory [17]. The inner dimensions of the modules between the driver piston and the resonator tube were modeled based on Table 1. For heat exchangers, although the heat exchanger housing was 2.54 cm, the thickness of the heat exchanger along the flow direction was 1.27 cm. The other portion of the housing was modeled as a duct. For comparison, some of the measured variables were used as target vectors [18] in DELTAE. These include the stack-end gas temperatures, the phase angle between pressure and velocity at the driver, the pressure and velocity amplitudes at the driver, and a zero enthalpy flux condition at the termination end. The guess vectors [18] used included the mean pressure at the driver, the amplitude and phase of the pressure at the driver, the volume velocity amplitude at the driver, and the heat transfer rates at both heat exchangers. The only system loss included in the model (automatically calculated in DELTAE) was the acoustic power dissipation in each module. In the model, the modules from the cold-side heat exchanger to the resonator tube were insulated.

Fig. 6 compares the COP obtained from DELTAE (COP_{DTE}) with the measured COP (COP_m). The 45° line in the Fig. represents perfect agreement. The data points are plotted with their relative uncertainties indicated by error bars. For small acoustic power, the measured COP was much higher than the predictions from DELTAE. As the acoustic power increased, the measured COP approached the DELTAE predictions. The large discrepancies for small acoustic power are believed to be caused by relatively high uncertainties in the cooling rate estimates for these conditions. As the acoustic power increases, the uncertainties decrease. The differences in performance for the two different mixtures were small.

4.2 Measurements with water flow through the cold-side heat exchanger

The overall system performance was measured with the cold-side heat exchanger connected to the secondary water loop. The water flow rate through the cold-side heat exchanger was held at 11 ml/s to ensure relatively large changes in water temperature and acceptable accuracy. For the hot-side, a flow rate of 40 ml/s was used to ensure effective heat removal. Such large water flow rate on the hot-side helped in maintaining a cold-side gas temperature near room temperature, thereby minimizing heat gain to the shell. Two different helium and argon mixtures (55 % helium and 44 % helium) were tested for gauge mean pressures of 0.345 MPa, 0.690 MPa, 1.034 MPa and 1.379 MPa. The COP of the thermoacoustic cooler was estimated by using Eq. (4). In this relation, the cooling rate is determined from an overall energy balance to account for heat gains to the thermoacoustic fluid from both the cold-side heat exchanger and the shell. The imbalance heat was estimated by Eq. (3) to compare the cooling rate estimated with the heat exchanger with the cooling rate directly estimated by using the measured inlet and outlet water conditions for the cold-side heat exchanger.

4.2.1 Results

Tables 3 and 4 show the data obtained for two different mixtures obtained on two different days. For all the measured data, the relative uncertainties in hot-side heat transfer rates, $\delta_R \dot{Q}_h$, were within 10 %. The imbalance heat was mostly within 15 %, and in all cases less than 20 %. The acoustic power delivered varied between 27.0 W and 76.1 W, with corresponding electroacoustic efficiencies varying between 17.8 % and 60.3 % depending on the mixture and the mean pressures. The electroacoustic efficiencies listed in Table 3 are smaller than those listed in Table 2 for 55 % helium and 45 % argon mixtures. This drop is mostly due to the fact that the stiffness of the leaf spring attached to the driver decreased over time following fatigue relaxation [11]. As the leaf spring aged, its stiffness decreased, and the mechanical resonance frequency of the driver dropped. This resulted in lower electroacoustic efficiencies for 55 % helium and 45 % argon mixtures, but higher values for 44 % helium and 56 % argon mixtures.

The cooling rates determined from an energy balance varied between 42.0 W and 87.4 W. The hot-side heat transfer rates were between 72.3 W and 153.7 W. The COP is plotted in Fig. 7 with respect to the acoustic power input for different mixtures and mean pressures. The COP's of the 55 % helium

Table 3. Measured data with water flow through cold heat exchanger (55 % helium -45 % argon mixture).

No	P_m (MPa)	$\dot{W}_{ac}$ (W)	η_{DR} (%)	$\dot{Q}_h$ (W)	$\dot{Q}_h - \dot{W}_{ac}$ (W)	COP	Tgh (K)	Tgc (K)	DR (%)	$\delta_R \dot{Q}_h$ (%)	Imb (%)
1	0.690	34.8	30.5	86.8	52.0	1.49	297.0	292.4	6.9	8.0	-2.6
2	0.690	45.5	31.0	108.3	62.9	1.38	297.3	291.9	7.7	6.4	-4.2
3	0.690	52.5	30.1	124.7	72.1	1.37	297.6	291.6	8.3	5.6	-6.3
4	0.690	66.4	28.9	153.7	87.4	1.32	298.2	291.2	9.4	4.6	-7.5
5	0.690	27.0	30.1	73.7	46.7	1.73	296.6	292.7	6.1	9.4	-13.4
6	0.345	28.7	20.0	72.3	43.6	1.52	296.5	292.6	8.5	9.6	-8.8
7	0.345	33.8	20.0	83.2	49.4	1.46	297.0	292.5	9.3	8.3	-5.9
8	0.345	39.8	17.8	107.1	67.3	1.69	297.3	292.0	10.5	6.5	-13.8
9	1.379	41.0	34.9	102.1	61.0	1.49	297.1	292.6	5.5	6.8	-18.2
10	1.379	32.9	37.6	86.6	53.7	1.63	296.9	292.8	5.1	8.0	-19.5
11	1.379	58.0	38.5	130.2	72.2	1.25	297.5	292.1	6.0	5.3	-12.0
12	1.379	65.7	36.7	139.3	73.6	1.12	297.9	291.8	6.1	5.0	-8.7
13	1.034	29.1	32.9	78.9	49.8	1.71	296.8	292.8	5.5	8.7	-12.6
14	1.034	40.2	34.4	101.9	61.7	1.53	297.1	292.3	6.3	6.8	-11.9
15	1.034	52.1	34.3	124.8	72.7	1.40	297.5	291.9	6.9	5.5	-11.1
16	1.034	61.9	34.4	138.8	76.8	1.24	297.8	291.6	7.1	5.0	-8.3

Table 4. Measured data with water flow through cold heat exchanger (44 % helium -56 % argon mixture).

No	P_m (MPa)	$\dot{W}_{ac}$ (W)	η_{DR} (%)	$\dot{Q}_h$ (W)	$\dot{Q}_h - \dot{W}_{ac}$ (W)	COP	Tgh (K)	Tgc (K)	DR (%)	$\delta_R \dot{Q}_h$ (%)	Imb (%)
1	0.690	43.8	59.9	100.3	56.5	1.29	297.3	292.0	7.8	6.8	2.3
2	0.690	56.0	57.9	125.9	69.9	1.25	297.5	291.4	8.7	5.5	-1.3
3	0.690	34.3	59.7	84.5	50.2	1.46	296.9	292.3	7.0	8.1	-2.1
4	0.690	67.3	54.3	146.7	79.4	1.18	298.0	291.1	9.5	4.7	-2.5
5	0.345	30.6	52.2	72.6	42.0	1.37	296.6	292.5	8.8	9.3	1.1
6	0.345	36.3	46.7	84.9	48.6	1.34	296.9	292.2	9.7	8.0	0.1
7	0.345	41.0	39.9	99.5	58.5	1.43	297.2	292.0	10.5	6.8	-3.0
8	0.345	44.6	36.4	113.1	68.5	1.54	297.4	291.8	11.1	6.0	-7.2
9	1.034	43.8	52.3	100.7	56.9	1.30	297.3	292.1	6.7	6.7	-5.0
10	1.034	58.8	54.1	124.1	65.3	1.11	297.9	291.8	7.4	5.4	-1.0
11	1.034	76.1	54.4	152.0	75.8	1.00	298.1	291.4	7.8	4.5	-1.8
12	1.034	33.6	52.2	84.3	50.7	1.51	296.7	292.5	6.0	8.0	-8.8
13	1.379	31.1	46.4	75.5	44.4	1.43	296.8	292.9	5.2	8.9	-5.6
14	1.379	41.0	47.5	94.1	53.1	1.29	296.9	292.5	5.7	7.1	-5.2
15	1.379	55.3	48.4	115.2	59.9	1.08	297.4	292.0	6.1	5.8	-2.2
16	1.379	72.6	49.1	140.4	67.8	0.93	297.8	291.7	6.4	4.8	-0.4

mixture were slightly higher than those for the 44 % helium mixture. They ranged between 0.93 and 1.71.

4.2.2 Comparisons with linear acoustic model predictions

The measured data were compared with the predictions from DELTAE. Fig. 8 shows the average COP with respect to the mean pressure for various acoustic power inputs. For both experimental results and predictions from DELTAE, the COP decreased as the acoustic power increased, except for the case of p_0=0.345 MPa. This trend is consistent with the measured data without water flow through the cold-side heat exchanger.

The COPs obtained from DELTAE were in reasonable agreement with the measured data for most cases, but they underpredicted the measured COPs for the gauge mean pressure of 0.345 MPa. The reasons for the discrepancies are not known. Additional experimental data would be needed to clarify this point, but such data could not be obtained with the current system because the electroacoustic efficiency of the driver was too low at this condition.

Fig. 9 compares the measured COP with the COP obtained

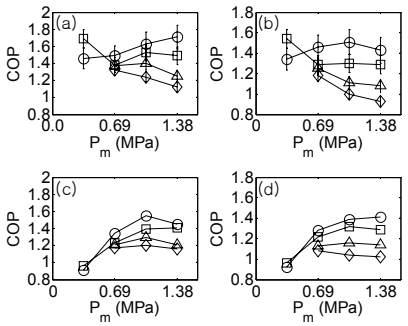

Fig. 8. COP vs. mean pressure. (a) and (c): 55 % helium and 45 % argon mixture, (b) and (d): 44 % helium and 56 % argon mixture. (a) and (b) are from measurement, and (c) and (d) are from DELTAE. For (a) and (c), O: $\dot{W}_{ac}$ =29W - 35W, : $\dot{W}_{ac}$ =40W – 45W, Δ: $\dot{W}_{ac}$ =52W – 58W, ◊: $\dot{W}_{ac}$ =62W – 66W. For (b) and (d), O: $\dot{W}_{ac}$ =31W - 36W, : $\dot{W}_{ac}$ =41W – 45W, Δ: $\dot{W}_{ac}$ =55W – 59W, ◊: $\dot{W}_{ac}$ =67W – 76W. All pressures are in gauge pressure. Experimental data are plotted with error bars.

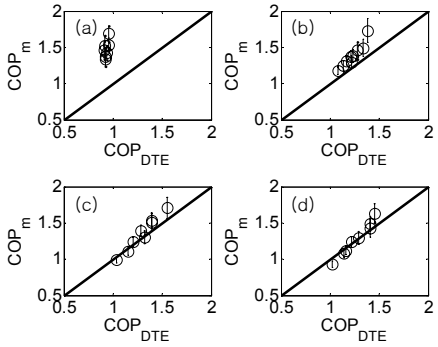

Fig. 9. Measured COP vs. COP from DELTAE. Solid line denotes the perfect agreement line. (a)P_m: 0.345 MPa, (b)P_m: 0.690 MPa, (c) P_m:1.034 MPa, (d) P_m: 1.379 MPa. Data points are plotted with error bars. All the data in Tables 3 and 4 are plotted. Data are plotted with error bars.

from DELTAE. The measured COP values are plotted with error bars representing their relative uncertainties. The 45° line again represents a perfect agreement. Except for 0.345 MPa, the agreement between them is reasonably good. For the data measured with water flow, the acoustic power input is relatively high and therefore the uncertainties are relatively small compared to the uncertainties of the data measured without water flow through the cold-side heat exchanger. Furthermore, the discrepancy between measured and simulated performance was reduced compared to results presented in the previous section.

5. Discussion

5.1 Water flow vs. no water flow

Fig. 10 shows the cooling rates and the cold-side stack-end gas temperatures with respect to the acoustic power input and the cooling rates with and without water flow through cold-

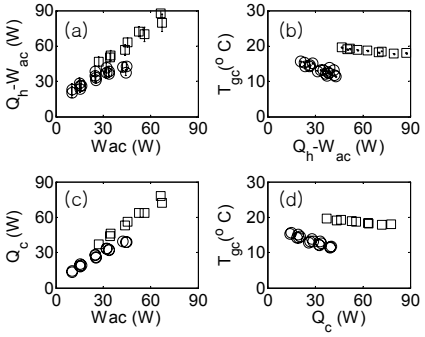

Fig. 10. Cooling rate and cold-side gas temperature vs. acoustic power and cooling rate. (a) and (b) are from measurement, and (c) and (d) are from DELTAE simulations. O: No water , : Water flow through cold-side heat exchanger. Qc's for (C) are DELTAE's predictions for the cold-side heat transfer rate. Experimental data are plotted with error bars.

side heat exchanger. Figs. (a) and (b) are from the measurements, and (c) and (d) are from DELTAE simulations. As expected, the cold-side stack-end gas temperatures without water flow were much lower than those with water flow through the cold-side heat exchanger. For about the same cooling power, 42 W, the cold-side gas-temperature reached about 284.9 K without water flow and 292.5 K with water flow. The reason why the cold-side gas temperatures are so different for these two cases can be partly explained by the overall heat transfer conductance of the heat transfer between the gas particles and the heat exchanger. In the absence of water flow in the cold-side heat exchanger, the overall heat transfer conductance should be less than with water flow. This reduces the heat transfer rate and also lowers the cold-side temperature for a fixed acoustic power input. Therefore, as shown in Fig 10(a), the cooling rate measured with water flow through the cold-side heat exchanger is larger than that measured without water in the heat exchanger. For the same cooling load, the cold-side stack-end gas temperature for the case of no water flow is lowered compared to the case with water flow, as shown in Fig. 10(b). The predictions from DELTAE (Figs. 10(c) and 10(d) showed similar patterns compared with the measured results (Figs. 10(a) and 10(b)). Although thermal losses and gains existing in the heat exchangers and stack are not considered in the current study, they will not affect the pattern of Fig. 10. The thermal losses and gains might affect the overall performances but they should not be large because the first law imbalances of the measured data are relatively small, and the deviations between the measured results and the DELTAE simulations are small.

Fig. 11 shows the stack temperature profile with respect to the distance from the driver piston with and without water flow through the cold-side heat exchanger for two similar cooling rates. The temperature profiles were obtained using DELTAE, with guess and target vectors as mentioned in Sec. 4.1.2. When there was no water in the cold-side heat exchanger, the temperature along the stack was nearly linear, i.e., a straight line connecting the hot and cold temperatures. In the

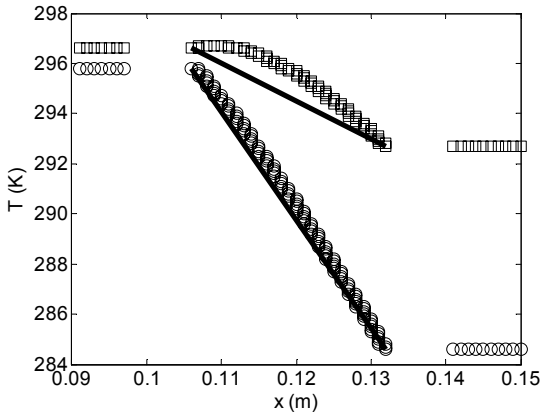

Fig. 11. Calculated stack temperature profile with and without water flow vs. distance from driver piston. O: No water ($\dot{Q}_c$ =42.8 W), : Water flow through cold-side heat exchanger ($\dot{Q}_c$ =46.7 W). Solid lines are straight lines connecting the hot and cold stack-end temperatures.

presence of water flow, the profile was not linear and the temperature gradient increased as the position moved between the hot and cold sides of the stack. When there was water flow in both exchangers, both stack-end temperatures were "anchored" to the hot and cold water temperatures and the most effective heat pumping effect (highest temperature gradient) occurred near the cold heat exchanger where the product of peak pressure amplitude and volume velocity were greatest. In fact, it is clear from Fig. 11 that only a portion of the stack near the hot heat exchanger participated in heat pumping when there was water flow. When there was no water flow in the cold heat exchanger, then the cold-end temperature was free floating and the system found an equilibrium condition that resulted in a more uniform heat pumping effect and temperature gradient. In this case, the entire stack participated in heat pumping.

5.2 Influence of stack-end temperature profile on performances

A mathematical analysis of the total energy flux equation [1] provides a basic understanding of the effects of stack temperature profiles on system performance. In the stack region, the total energy flux can be expressed as [18]

$$\dot{H} = \frac{1}{2}\mathbf{Re}\left[p_1 \tilde{U}_1 \left(1-\left(A+Bi\right)\right)\right] + |U_1|^2 \frac{dT_m}{dx} X \,, \tag{5}$$

where $\dot{H}$ is the total energy flux, p_1 is the complex acoustic pressure, U_1 is the complex volume velocity, dT_m / dx is the stack temperature gradient, Re represents the real part, '~' denotes a complex conjugate, and A, B and X are

$$A = \mathbf{Re}\left[\frac{f_\kappa - \tilde{f}_\nu}{(1-\tilde{f}_\nu)(1+\varepsilon_s)}\right]\frac{T_m \beta}{(1+\sigma)}, \tag{6}$$

$$B = \mathbf{Im}\left[\frac{f_\kappa - \tilde{f}_\nu}{(1-\tilde{f}_\nu)(1+\varepsilon_s)}\right]\frac{T_m \beta}{(1+\sigma)}, \tag{7}$$

and

$$X = \frac{\rho_m c_p}{2\omega A_{fluid}(1-\sigma)|1-f_\nu|^2} \times \mathbf{Im}\left[\tilde{f}_\nu + \frac{(f_\kappa - \tilde{f}_\nu)(1+\varepsilon_s f_\nu / f_\kappa)}{(1+\varepsilon_s)(1+\sigma)}\right] - \frac{(AK + A_{solid}K_{solid})}{|U_1|^2}, \tag{8}$$

respectively. In Eqs. (6)-(8) T_m is the temperature, σ is the Prandtl number, β is the thermal expansion coefficient, ρ_m is the density, c_p is the specific heat, ω is the angular frequency, A is the cross-sectional area, K is the thermal conductivity, the subscripts ν and κ represent viscous and thermal, respective, f is the spatially averaged thermoviscous function, and ε_s is a correction for thermal properties of the solid wall [1]. Note that $\dot{H}$ is negative for cooling, with the positive direction defined as oriented from the driver to the cold side heat exchanger, with heat transferred from the cold-side heat exchanger to the hot side heat exchanger.

For time harmonic signals, Eq. (5) can be written as

$$\dot{H} = \dot{W}_{ac}\left((1-A) + B\tan\phi\right) + |U_1|^2 \frac{dT_m}{dx} X, \quad \left(\phi \neq \pm\frac{\pi}{2}\right), \tag{9}$$

where, ϕ is the phase angle of Z_{ac}.

Dividing both sides of Eq. (9) by $-\dot{W}_{ac}$ yields

$$\frac{\dot{H}}{-\dot{W}_{ac}} = COP = -\left[(1-A) + \tan\phi\left(B + \frac{X}{|Z_{ac}|\sin\phi}\frac{dT_m}{dx}\right)\right], \tag{10}$$

where COP represents the coefficient of performance.

In Eq. (6), the magnitude of A is always between 0 and 1. $T_m\beta$ is 1 for ideal gases. ε_s is known to be near zero in most cases [18]. The real parts of the thermoviscous functions, f_κ and f_ν are always positive and similar in magnitude. The imaginary parts of these functions are always negative and similar in magnitude. This means that the magnitudes of the real and imaginary parts of $f_\kappa - \tilde{f}_\nu$ are much smaller than those of $1-\tilde{f}_\nu$. Therefore, the magnitude of the real part of the term in the bracket should be always less than 1, and $(1-A)$ in Eq. (10) should be always positive.

In Eq. (8), it can be observed that X is always negative. If we neglect the last term for heat conduction and ε_s because they are small compared with other terms and usually negligible [18], then Eq. (8) becomes

$$X \approx \frac{\rho_m c_p}{2\omega A_{fluid}(1-\sigma)|1-f_\nu|^2}\mathbf{Im}\left[\frac{\sigma\tilde{f}_\nu + f_\kappa}{(1+\sigma)}\right]. \tag{11}$$

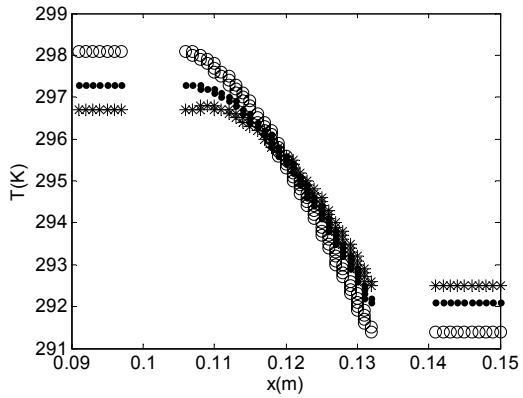

Fig. 12. Simulated stack temperature profile with water flow vs. distance from driver piston for various acoustic power inputs. *: $\dot{W}_{ac}$ = 33.6 W, •: $\dot{W}_{ac}$ = 43.8 W, and O : $\dot{W}_{ac}$ = 76.1 W.

The Prandtl number, σ, is about 0.4 for 55 % helium and 45 % argon mixture and varies between 0.2 and 0.67 for different gases normally used for thermoacoustic coolers [19]. Again, the imaginary part of the thermoviscous function, f, is known to be negative [1], and the magnitudes of the imaginary parts of f_ν and f_κ are similar. Therefore, the numerator of the term in the bracket is negative, and X is always negative. This means that the dT_m/dx term in Eq. (10) is always positive at the cold end of the stack, because dT_m/dx is always negative at the cold end of the stack.

From these results, B should be negative to yield a positive COP. Because the signs of B and the dT_m/dx term in Eq. (10) are opposite, when the magnitude of dT_m/dx decreases, the COP becomes larger and when the magnitude of dT_m/dx increases the COP becomes smaller if other variables remain unchanged. Therefore, if we compare the slopes of the temperature profiles of data points at the cold-end of the stack, the steeper slope (larger in magnitude) should yield smaller COP and the milder slope (smaller in magnitude) should yield a higher COP. This is true only when other variables in Eq. (10) are the same. Such variables include the stack-end temperatures, stack lengths, mean pressures, gas mixtures, acoustic impedances, and others.

For the two data sets in Fig. 11, the COP is greater with water flow than that without water flow based on Tables 3 and 2, respectively. It would have been greater if the temperature profile had been linear, but a linear stack temperature profile cannot be achieved for the given temperature span without reducing the stack length.

Fig. 12 shows the stack temperature with respect to the distance from the driver piston with water flow through the cold-side heat exchanger for various acoustic power inputs. The temperature profiles were obtained from DELTAE. As the acoustic power increased, the stack temperature difference increased and the COP decreased. For the acoustic power of 33.6 W, the temperature profile was very non-linear between the hot and cold stack-end temperatures. As the acoustic power increased, the temperature span across the stack increased and the stack temperature profile became more linear. For a given stack length, there exists a temperature span where the temperature profile is nearly linear. Non-linear profiles reduce COP because the slope of the stack temperature profile at the cold end of the stack becomes steeper, as described earlier. But the resulting COP is not solely due to the temperature profile. Other factors such as viscous dissipation, heat conduction loss along the stack, stack position, and others are also significant.

6. Conclusions

The performance of a standing-wave thermoacoustic cooler was investigated. Comparisons were made between measured data and predictions from linear acoustic theory for various mean pressures, acoustic powers, and gas mixtures. In general, the experimental data were in good agreement with theoretical predictions. In comparison to the performance without water flow through the cold-side heat exchanger, higher COPs were obtained in presence of water flow because of a reduced stack temperature difference due to higher cooling load and overall heat transfer conductance. Temperature profiles along the stack obtained from DELTAE showed that the temperature profiles with water flow through the cold heat exchanger were non-linear and resulted in a slight decrease in the system performance.

If the temperature span is relatively too small compared to stack length, the temperature profile becomes non-linear, leading to a significant reduction in COP. The results described in this paper highlight that standing wave thermoacoustic coolers must be operated at or near their design temperature span for optimal system performance.

Acknowledgment

The authors express their thanks to the Office of Naval Research (ONR), and the Air-Conditioning and Refrigeration Technology Institute (ARTI) for their financial support. The contribution of the Herrick Laboratories Technical staff is also gratefully acknowledged. Moreover, among the many who helped with this project, we are deeply indebted to Fred Keller of Carrier and Steve Memory of Modine for their help and support.

Nomenclature

A	:	Surface area or cross sectional area
A_{fluid}	:	Fluid area in stack
A_{solid}	:	Solid area in stack
COP	:	Coefficient of performance
c_p	:	Specific heat
DR	:	Peak-to-mean pressure ratio
f	:	Spatially averaged thermo-viscous loss function
Im	:	Imaginary part
Imb	:	Imbalance heat

h : Heat transfer coefficient
$He\,\%$: Percentage of helium in helium – argon mixture
$\dot{H}$: Total energy flux
k : Thermal conductivity
p_1 : Complex acoustic pressure
P_m : Mean pressure
$\dot{Q}_h$: Hot-side heat transfer rate
$\dot{Q}_c$: Cold-side heat transfer rate
Re : Real part
R_{tw} : Thermal resistance of tube wall
T_{gc} : Cold-side stack-end gas temperature
T_{gh} : Hot-side stack-end gas temperature
T_w : Temperature of water
T_m : Mean temperature
UA : Heat transfer conductance
U_1 : Complex volume velocity
$\dot{V}_w$: Water volume flow rate
$\dot{W}_{ac}$: Acoustic power
Z_{ac} : Acoustic impedance
β : Thermal expansion coefficient
γ : Specific heat ratio
Δ : Difference
δ : Uncertainty
$\delta_R \dot{Q}_h$: Relative uncertainty in hot-side heat transfer rate
ε_s : Correction for thermal properties of solid wall
η_{DR} : Electroacoustic efficiency
η_0 : Overall fin efficiency
ρ_w : Density of water
σ : Prandtl number
ω : Angular frequency
ϕ : Phase angle of Zac

References

[1] G. W. Swift, Thermoacoustics: A unifying perspective for some engines and refrigerators, Acoustical Society of America, New York, USA (2002).

[2] T. J. Hofler, Thermoacoustic refrigerator design and performance, Ph.D. dissertation, Physics department, University of California, San Diego, CA, USA (1986).

[3] S. L. Garrett, J. A. Adeff and T. J. Hofler, Thermoacoustic Refrigerator for Space Applications, J. of Thermophysics and Heat Transfer 7 (4) (1993) 595-599.

[4] T. J. Berhow, Construction and performance measurement of a portable thermoacoustic refrigerator demonstration apparatus, M.S. thesis, Physics department, Naval Postgraduate School, Monterey, CA, USA (1994).

[5] M. E. H. Tijani, Loudspeaker-driven thermo-acoustic refrigeration, Ph. D. dissertation, Technische Universiteit Eindhoven, Eindhoven, Netherlands (2001).

[6] S. C. Ballister and D. J. McKelvey, Shipboard electronics thermoacoustic cooler, Master's thesis, Physics Dept., Naval Postgraduate School, Monterey, CA, USA (1995).

[7] M. E. Poese and S. L. Garrett, Performance measurements on a thermoacoustic refrigerator driven at high amplitudes, J. Acoust. Soc. Am., 107 (2000) 2480-2486.

[8] S. L. Garrett, Next-generation thermal management, Slides used for Presentation, Dallas/Ft. Worth, October 2002.

[9] I. Paek, J. E. Braun and L. Mongeau, Evaluation of suitable applications for thermoacoustic coolers, Int. J. Refrig., 30 (2007) 1059-1071.

[10] J. Wheatley, T. Hofler, G. W. Swift and A. Migliori, An intrinsically irreversible thermoacoustic heat engine, J. Acoust. Soc. Am., 74 (1983) 153-170.

[11] I. Paek, Performance characterization of thermoacoustic cooler components and systems, Ph.D. dissertation, School of Mechanical Engineering, Purdue University, West Lafayette, IN, USA (2005).

[12] G. A. Yarr and J. A. Corey, Linear Electrodynamic Machine, US Patent No. 5389844. Feb. 14 (1995).

[13] I. Paek, L. Mongeau and J.E. Braun, A method for estimating the parameters of electrodynamic drivers in thermoacoustic coolers, J. Acoust. Soc. Am., 117 (2005) 185-193.

[14] I. Paek, J. E. Braun and L. Mongeau, Characterizing heat transfer coefficients for heat exchangers in standing wave thermoacoustic coolers, J. Acoust. Soc. Am., 118 (2005) 2271-2280.

[15] F. Incropera and D. Dewitt, Fundamentals of heat and mass transfer, Wiley and Sons, New York, USA (1996).

[16] J. R. Taylor, An Introduction to Error Analysis, University Science Books, CA, USA (1997), Eq. (3.47).

[17] W. C. Ward and G. W. Swift, Design environment for low amplitude thermoacoustic engines (DeltaE), J. Acoust. Soc. Am. 95 (1994) 3671-3672. Software and user's guide available either from the Los Alamos thermoacoustics website at www.lanl.gov/thermoacoustics/(date last viewed 10/31/2008) or from the Energy Science and Technology Software Center, US Department of Energy, Oak Ridge, TN, USA.

[18] W. C. Ward and G. W. Swift, DELTAE Tutorial and User's Guide Version 5.1, Los Alamos National Laboratory, , Los Alamos, NM, USA (2001).

Insu Paek received the B.S. in Mechatronics Engineering from Kangwon National University, Chuncheon, Korea, in 1997, and the M.S. in Mechanical Engineering from the University of Texas at Austin, USA, in 2000. He received the Ph. D. in Mechanical Engineering from Purdue University, USA, in 2005. He worked as a postdoctoral researcher at Purdue University and McGill University in 2006 and 2007. He is currently an assistant professor in the Department of Mechanical and Mechatronics Engineering, Kangwon National University, Korea. His research activities are in thermoacoustic cooling, solar powered absorption cooling, and wind power generation.

Luc Mongeau received the B.S. and M.S. in Mechanical Engineering from the University of Montreal, QC, Canada, in 1984 and 1986, respectively, and the Ph. D. in Acoustics from Pennsylvania State University, University Park, USA, in 1990. He is currently a professor in the Department of Mechanical Engineering at McGill University, Montreal, QC, Canada. He has published over 50 archival journal publications on various topics related to acoustics and noise control. His research activities are in the flow and turbomachinery noise areas, as well as in the areas of voice production, and thermoacoustic refrigeration.

James E. Braun received the B.S. in Mechanical Engineering from the University of Massachusetts, USA, in 1976, and the M.S. and Ph. D. degrees in mechanical engineering from the University of Wisconsin, Madison, USA, in 1980 and 1988, respectively. He is currently a professor in the Department of Mechanical Engineering, Purdue University, West Lafayette, USA. Professor Braun's research combines the use of computer modeling, optimization, and experiments to study and improve the performance of thermal systems. He has published over 140 papers. Professor Braun is currently an associate editor for the international journal of HVAC&R Research.